Characterising the Long-Term Variability in Blazars

JHE Thiersen

orcid.org 0000-0002-4024-3280

Dissertation accepted in partial fulfilment of the requirements for the degree *Master of Science in Astrophysical Science* at the North-West University

Supervisor: Prof M Boettcher

Graduation May 2020

26559226

Abstract

Most research on blazar variability focuses on individual flares to explain acceleration and radiation mechanisms and improve on current models. These short-time events (being minutes, hours, or days) might not be representative of the underlying mechanisms causing small-amplitude variability and/or continuous emission which is present most of the time. We will therefore investigate long-term (months to years) variability of blazar emission in the framework of current leptonic blazar models. For this purpose, we introduce generated time-dependent parameter variations which are based on typical Power Spectral Densities (PSDs) associated with the variability of accretion flows. The PSDs from the resulting light curves are analyzed and compared to one another, as well as the PSD of the input variation. Correlations between light curves are also investigated to aid identification of characteristic variation patterns associated with leptonic models. The resulting multi-wavelength PSDs were found to follow the input variation PSD trend closely, however, it presented no clear distinctions between the varied parameters. The multi-wavelength cross-correlations showed significant differences among the varied parameters. We therefore conclude that the PSDs are plausible candidates for extracting the variational trends of variability progenitors while multi-wavelength cross-correlations would be a plausible diagnostic for identifying radiative mechanism characteristics as well as the varying quantity in the emission region.

Keywords: Active Galactic Nuclei; Blazar Variability; Multi-Wavelength; Blazar Modelling; Time Series Analysis

Acknowledgements

Most thanks go to both my supervisors Prof. Markus Böttcher and Dr. Michael Zacharias. I am truly grateful for their support, encouragement and the opportunities I was given while working with them. I have learned so much from them both and look forward to learn even more in the future. With respect to the write-up itself I thank them for all the proofreading, comments, suggestions, etc.

I also want to give special mention to Dr. Sunil Chandra and Hester Schutte for their willingness to engage in discussions with me when I was in a tough spot. They gave me the little inspiration and motivation I often needed. Additionally I want to thank Hester for all her help near the end. For advice and suggestions while developing the code, even if it was not included into the final project, I want to thank the following people: Dr. Zacharias, Dr. Chandra, Dr. Zorawar Wadiasingh, Dr. Patrick Killian and Mr. Bertie Seyfert.

I would lastly like to generally thank everyone at the Centre for Space Research (CSR), North-West University for all their support.

List of Figures

List of Tables

Contents

Chapter 1

Introduction

Since the dawn of mankind humanity has been intrigued by the brilliance and mystery of our universe. It was not until Edwin Hubble's discovery of galaxies (previously thought to be nebulae) far outside the span of the Milky Way in 1926 (Hubble, 1926) that our view of the universe was severely challenged. This breakthrough also paved the way for many astronomy-related branches of science to make significant leaps in progress. Furthermore, follow-up studies and investigations on galaxies found that there are a vast variety of different galaxies in our universe.

The basic important characteristics of galaxies are that they are gravitationally bound extragalactic objects made up of mostly gas, dust, stars and dark matter. It is widely accepted that every galaxy possesses at least one supermassive black hole (SMBH; $M > 10^8 M_\odot$) at its centre responsible for the gravitational binding which largely contributes to its observed structure (Gültekin et al., 2009; Magorrian et al., 1998).

Galaxy taxonomy can be quite extensive and involved. Early classifications of galaxies were done based on appearance in the optical spectrum. With advancement in technology and science new observational instruments were developed with which observations of galaxies were extended to the whole electromagnetic spectrum. These include telescopes in radio, more in optical and γ-rays, satellites in infrared, ultraviolet emission, X-rays and γ-rays. This along with the improvement of observational precision and accuracy has lead to more extended classifications possibilities based on properties over the entire emission spectrum. Most galaxies show emission that represents the emission from its collection of stars. However, active galaxies are galaxies that emit radiation that cannot be explained by starlight alone and is often much brighter than the emission from the combined starlight. They are among the brightest objects in the universe.

1.1 Active Galactic Nuclei

Active galaxies are galaxies for which the central region harbouring the SMBH emits bright multi-wavelength radiation comparable in flux to their host galaxy, but often outshining it. These central regions are called Active Galactic Nuclei (AGN).

Like galaxies there are multiple types of AGN that are classified based on features in their emission. The differences are mostly attributed to the host galaxy environment and partially to the orientation with respect to our line of sight.

The unified model for AGN (Urry and Padovani, 1995) attempts to connect most common features and similarities found in all AGN from observations. This model proposes that AGN consist of several structural components that have different radiative profiles associated to them. Apart from a SMBH and accretion disc in the central region, these structural components (which will be discussed shortly) might not be present or visible in every AGN. This combined with the possibilities of orientation with respect to our line of sight results in a wide variety of AGN. The structural components of AGN from smallest to largest size scales are:

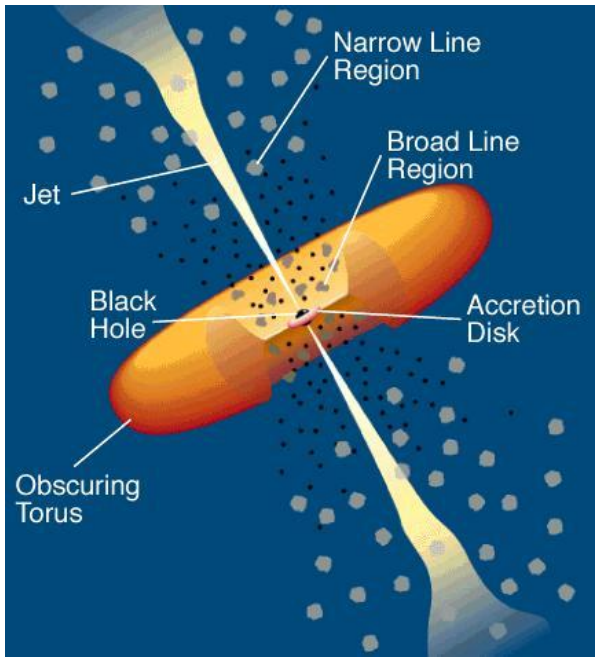

Figure 1.1: Representation of unified model for AGN (Urry and Padovani, 1995).

- A SMBH actively accreting matter from an accretion disc surrounding it in a volume with radius from a few up to thousands of R_S (Schwarschild radius) where $R_s = \frac{2GM}{c^2}$. This is thought to be the power house of the emission from AGN

although the exact mechanism for achieving this is not well understood. In principle the particles in the accretion disc convert gravitational potential energy into kinetic and thermal energy as they approach the black hole (BH). Angular momentum is also transferred among the particles which is needed to break orbital motion and allow matter to fall in onto the BH. Typically the emission spectrum of the accretion disc peaks in UV with its temperature being $T \approx 10 \times 10^5\,\mathrm{K}$.

- A corona is in the vicinity of the SMBH and the accretion disc. The corona upscatters emission from the accretion disc. Therefore it is a source of high-energy (HE) X-ray photons.

- Farther out on subparsec scales is the Broad Line Region (BLR) which is a collection of fast moving gas clouds. These clouds emit line emission that is broadened in the detected spectrum by Doppler-boosting due to cloud motion being a significant fraction of light speed, $v_{\mathrm{BLR}} \approx 10^{-1}c$.

- A few parsec farther is the Narrow Line Region (NLR) which is similar to the BLR only with lower gas cloud speeds and thus narrow line emission spectra. The speeds of these clouds are approximately $v_{\mathrm{NLR}} \approx 10^7\ \mathrm{cm \cdot s^{-1}}$.

- All previously mentioned components are radially surrounded by what is referred to as a Dusty Torus (DT) at a few parsec from the central region. It consists of thermal dust with a temperature of $T \approx 10 \times 10^3\,\mathrm{K}$, its emission spectrum peaking in infrared. However, the significance of the DT is not its emission, but its role in effectively obscuring the central region. Depending on a galaxy's orientation relative to our line of sight, the central region (BH and accretion disc) or additionally the BLR is obscured. Therefore one of the core explanations of the differences in AGN emission is the degree of obscuration by the DT.

- The final consideration and key difference among AGN are streams of relativistic particles ejected along the spin axis of the central region called relativistic jets. These jets manage to extend out to kpc/Mpc scales while remaining collimated. This is a feature of only a portion (10%; Della Ceca et al. (1994); Kellermann et al. (1998)) of all AGN, though. These jets exhibit extreme radiative power emitting from radio up to very high-energy γ-rays. There is currently no explanation as to why these jets occur in only a portion of the AGN population. How jets are launched and maintained for their whole extent is also an unsolved mystery. Since jets have such a dominant impact on the emission the presence of this feature is

useful for classification and splits AGN into radio-loud (jets present) and radio-quiet (jets absent) AGN.

Applying the unified model to the different types of galaxies we see that jets are absent from most AGN in Seyfert galaxies. The distinction between the Type 1 and 2 Seyferts is made on the basis of broad line emission. In the model the broad emission is obscured when the DT is in the line of sight which occurs for large angles compared to the spin axis. This obscuration occurs in Type 2 Seyferts and not in Type 1 Seyferts.

Fanaroff-Riley (FR) I and II galaxies and blazars are good examples of the role played by orientation for radio-loud sources. The relativistic material inside the jets of these galaxies are beamed in a cone where the opening angle is approximately $\frac{1}{\Gamma}$ with Γ the bulk Lorentz factor of the relativistic material. For FR I and II galaxies the angle between the jet axis and the line of sight $\theta_{\rm jet}$ is larger than the beamed cone opening angle, $\theta_{\rm jet} \gg \frac{1}{\Gamma}$. In the case of blazars the line of sight is within this beaming cone, $\theta_{\rm jet} \lesssim \frac{1}{\Gamma}$ leading to highly Doppler-boosted emission.

1.2 Blazars

This thesis is only concerned with one class of AGN, blazars. For blazars, one relativistic jet is aligned closely to our line of sight (within $\sim 10^{\circ}$). Therefore from the unified model it can be concluded that we are staring almost perfectly down the jets and observing the central region directly. However, due to the relativistic motion of the jet highly Doppler-boosted jet emission dominates most of the spectrum. If the emission contributions from the rest of the AGN are too faint it can be negligible simplifying investigations to only jet physics and radiative processes as is often the case.

Blazars have a characteristic double-humped power emission spectrum as seen in their spectral energy distribution (SED). The low-energy hump has typical ranges from radio to ultra-violet/X-rays while the high-energy hump from X-rays up to very high-energy (VHE) γ-rays. The two models used to describe and predict blazar emission are the leptonic and hadronic model (Böttcher et al., 2012, 2013). The most important differences between these models are the particle species responsible for the radiation. Consequently, different particles also implies different radiation mechanisms. In both models the low-energy hump is attributed to synchrotron radiation from relativistic electrons. The high-energy hump is explained by Inverse Compton (IC) scattering in the leptonic model while in the hadronic model it is considered to be consequence of photo-pion and pair production and synchrotron radiation from protons and mesons. The production of VHE neutrinos is also predicted by the hadronic model. Extensive

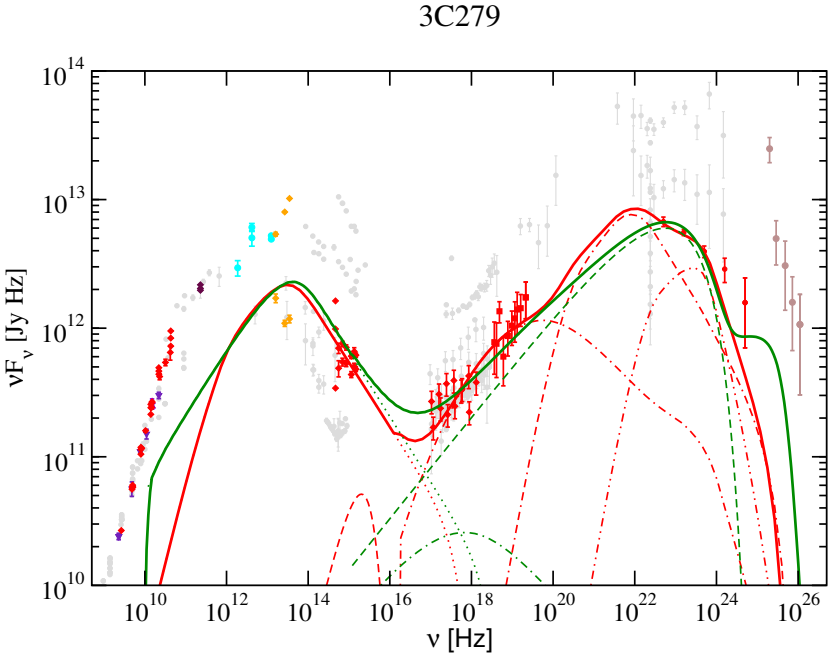

Figure 1.2: SED of 3C 279 with fits for the leptonic (solid red) and hadronic (solid green) models. Plot provided by Böttcher et al. (2013).

research is done to confirm whether blazars are the producers of extra-galactic neutrinos (IceCube Collaboration et al., 2018; Aartsen et al., 2015).

1.3 Variability

Besides the double-hump in the energy spectrum of blazars, multi-wavelength variability is another ubiquitous characteristic of all AGN. In fact, multi-wavelength flux variability is even more extreme in jets with time scales down to a few minutes compared to non-beamed AGN (Aharonian et al., 2007, 2009). This also implies that the variability of blazars is most likely due to variations occurring in the jets themselves. The ubiquity could be indicative of a relation with some intrinsic property of AGN.

The origin and cause of the variability is still unknown, but there are models which attempt to explain it with various amounts of success.

Internal shock models propose the development and propagation of shocks through the jets (e.g. Baring et al., 2017; Blandford and Eichler, 1987; Böttcher and Dermer, 2010). In principle particles are accelerated by crossing the shock front multiple times. The energy gain from each crossing of the shock front scales exponentially with time.

Turbulence and magnetic reconnection are also investigated as a variability and acceleration progenitor (e.g. Guo et al., 2016; Kagan et al., 2015; Nalewajko et al., 2015).

Turbulence is a ubiquitous part of every fluid which in plasma can have interesting consequences on the magnetic field. Specifically it can cause instabilities in a plasma that can trigger magnetic reconnection. Magnetic reconnection is the realignment of the magnetic field topology by the release of magnetic energy from a higher energy configuration to a lower energy one. This event converts the magnetic energy to thermal and kinetic energy in the plasma and provides an efficient way to accelerate particles (Zweibel and Yamada, 2009).

External interference is a very logical argument to explain variability, especially some cases of variability tied to flares (distinctly different compared to long-term trends). Specific examples of this could be ablation of a cloud (Zacharias et al., 2017, 2019), stars or stellar winds in the jet (Araudo et al., 2013; Barkov et al., 2010, 2012) increasing particle injection and/or the jet slamming into a cloud resulting in a shock. It should be noted that flares are not necessarily tied to external influences. It can also be caused by instabilities and/or inhomogeneities in the jets.

This work does not focus on any model involving a specific, usually external event that drives the variability. Instead variability is simulated as a variation of intrinsic emission region properties in jet physics and the reaction of the emitted radiation is analysed.

Variability presents one with valuable information on the time scales of radiative mechanisms. An important quantity that can be derived from these time scales is the size of emission regions. For variability in a considered waveband with observed minute time scales $t^{\mathrm{obs}} \sim 10^2$s the emission region size has to be of the order of the light crossing time scale $R_{\mathrm{em}} \sim \frac{c\delta t^{\mathrm{obs}}}{1+z} = \frac{\delta}{1+z} 3 \times 10^{12}$cm where δ is the Doppler factor and z the redshift of the source. Often evidence is found that the sizes of the emission regions for different wavelengths differ, with the higher energy radiation coming from the smallest regions. It is thus reasonable to conclude that the origin and energy of radiation depends on its location in the AGN.

Variability is not exclusive to AGN. It is also found in X-ray binaries for example. X-ray binaries are sources in which a compact object and companion star are locked in orbit that produces relatively intense X-ray spectra. In these systems it is common for matter from the companion star to fall onto the compact object, either a white dwarf, neutron star or BH, and produce an accretion disc with a jet. Variability detected in X-ray binary sources was found to exhibit the same behaviour as that of blazars characterised as red noise (e.g. Chatterjee et al., 2012; Cui, 1999; Goyal et al., 2018; Kataoka et al., 2001; Trippe et al., 2011; Van der Klis, 2004), where the Power Spectral Densities follow a power-law at lower frequencies.

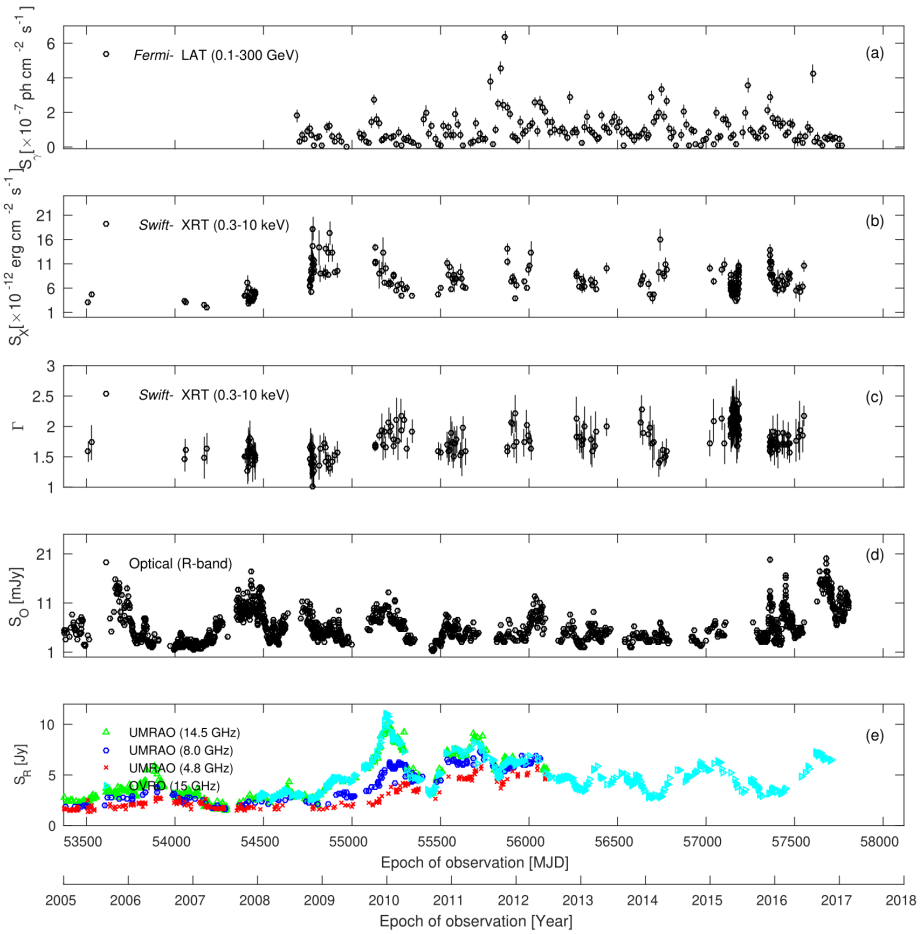

Figure 1.3: Multi-wavelength variability in the observations of BL Lac object OJ 287 from 2005 to 2018 (Goyal et al., 2018). Energy ranges as shown in the legends.

1.4 Overview

Research that study the variability of blazar emission mostly focuses on flaring events modeled by acceleration and radiation mechanics to explain the phenomenon and improve our understanding of the physics. These flaring events might not be representative of the underlying mechanisms responsible for the small-amplitude fluctuations that are present for much longer than the flares themselves. This thesis therefore investigates variability from the framework of a current leptonic blazar emission model for which variations are introduced to mimic changes that lead to variability in the emission. These variations are created by changing parameters in the leptonic model over time. Different parameters varied over time will affect the model in different ways. This then produces different variability signatures which is analyzed for distinctive characteristic features of the different varying parameters. This work has already been published in

a proceedings paper (Thiersen et al., 2019). Characterised variability signatures could possibly be a diagnostic tool to identify the underlying changing parameters when analyzing observational data.

The following chapters will elaborate on some of the content in this introduction as well as give an in-depth discussion of important, relevant concepts in this work. Chapter 2 discusses some investigative tools for variability. An in-depth discussion of the theoretical models used in this work is found in Chapter 3. Results are presented and discussed in Chapter 4 with a summary and conclusions in Chapter 5. An outlook on future work is also given in Chapter 6.

Chapter 2

Characterisation of Variability

Variability is the changes over time detected in the fluxes of astrophysical objects. Astrophysical objects that involve some accretion mechanism, that is material falling onto a compact object e.g. binary systems and AGN, exhibit similar variability signatures.

The variability of a system can be investigated with multiple methods. This thesis employs Power Spectral Densities and Cross-correlations to analyse the variability in light curves. These methods are described in this chapter.

2.1 Power Spectral Densities

The Power Spectral Density (PSD) of any time series is an expression of the power of the series in frequency space. In the case of variable light curves we can interpret their PSDs as the amount of emission power per temporal frequency which is a measure of the magnitude of change that occurs on different time scales.

Obtaining the PSD of a light curve is a matter of calculating the square of the periodogram (the Fourier transform/counterpart of a time series). This work has the benefit of using generated discrete data that are evenly-spaced in time. This allows for the direct use of the Fast Fourier Transform (FFT) to calculate each and every periodogram to obtain the PSD.

In systems that have some accretion mechanisms it is often found that the PSDs exhibit a phenomenon known as red noise. That is, the power and temporal frequency has a power-law proportionality, $P \propto f^{-\alpha}$, consequently leading to large-scale changes over long periods of time, and contrarily small-scale changes in emission over short periods of time. Another feature that is common in binary systems is a Quasiperiodic Oscillation (QPO). This is a surge in power at a particular temporal frequency in the PSD of one or more wavebands. Such a feature is an indication that there is

a mechanism present with a periodic nature. In general QPOs are not detected in blazars, but exceptions to this generalisation do exist.

2.2 Cross-correlations

Cross-correlations are a powerful tool in signal processing, employed to determine similarity and time delays when comparing light curves. Again due to the benefit of having evenly-spaced data in this work it is most convenient to use the classical correlation function (Papoulis, 1962; Bracewell, 1965; Oppenheim and Schafer, 1975). Given time series $a(t)$ and $b(t)$ the cross-correlation between them is computed with the Correlation Function (CF):

$$\mathrm{CF}(\tau) = \frac{\mathrm{E}\{[a(t) - \bar{a}][b(t+\tau) - \bar{b}]\}}{\sigma_a \sigma_b} \tag{2.1}$$

$\mathrm{E}\{f\}$ is the expectation value which in this work evaluates to the average of the expression f in braces, $\bar{i}$ represents the mean and σ_i is the standard deviation of the considered time series where $i = a, b$.

The cross-correlation, $\mathrm{CF}(\tau)$, only produces results within the range [-1, 1]. The value of τ at a maximum/minimum in $\mathrm{CF}(\tau)$ shows the time lag between the series for their correlation/anti-correlation.

In the context of blazar emission this calculation computes the time lags between light curves of different wavebands. Time lags that arise from different wavebands exhibiting similar variability patterns can be an indication of the same type of particles and mechanism with an energy dependence. The high-energy particles are more efficient emitters than low-energy particles; thus the low energy component is delayed compared to the high energy component since the low energy particles emit on longer time scales. More details on emission time scales are discussed in Chapter 3.

Besides time lags the similarity of variability in different light curves is tested. Cross-correlation with maxima/minima of the order ± 0.9 would be considered a strong correlation or anti-correlated. Maxima/minima of the order ± 0.5 are weak correlations showing that the varibility patterns are not perfectly identical. This is demonstrated with synthetic light curves in Figure 2.1. These light curves were generated with the algorithm of Timmer and König (1995) which is discussed in detail in Section 3.4.

In the top row of Figure 2.1 the blue and orange cross correlations are strong: maxima/minima at $\sim \pm 1$. Thus the variability in blue and orange light curves are strongly related. This is especially true for blue since it is the cross correlation with

itself which will always produce a maximum of 1 at $t = 0$. The green cross correlation is weaker, but is still considered significant. The green and orange cross correlations also show time delays. The negative delay in green indicates that the variability in the green light curve precedes the variability in blue. The inverse is true for variability in orange which has a positive delay and therefore is preceded by the variability in blue.

In the bottom row uncorrelated light curves are presented. The cross correlation in orange is never stronger than ± 0.25 and does not have distinctive minima/maxima which indicates insignificant similarity between the variability in blue and orange. The blue and orange light curves are therefore uncorrelated.

Figure 2.1: Demonstration of cross correlations of synthetic light curves. The color of the lines in the cross correlation plots (*right*) indicate which light curve was cross correlated to the blue curves (*left*). Therefore the blue cross correlation shows a correlation with itself. *Top:* Variability in these synthetic light curves are similar to some extent. *Bottom:* Variability is dissimilar for these synthetic light curves.

Chapter 3

Leptonic Variability model

In this thesis variability progenitors are assumed to be variations of properties in blazars' emission regions. Multi-wavelength variability is thus modelled by varying one of these properties in time in the framework of the leptonic emission model of Diltz and Böttcher (2014). The variability in the light curves produced by the model is then studied and analysed. This work exclusively focuses on the leptonic scenario for blazar emission as a first step to a comparitive study.

Similar work was done by Finke and Becker (2014) and Mastichiadis et al. (2013). In the work by Finke and Becker (2014) they analytically explored electron transport in the emission region in the Fourier domain. Mastichiadis et al. (2013) studied the variability signatures of lepto-hadronic models using Mrk 421 as a case study.

The two requirements to model variability in this way are: (1) a method for systematically generating multiple variations as time series and (2) a time-dependent leptonic blazar emission model. A brief overview of the important radiation mechanisms of leptonic emission is given in Section 3.1. In Section 3.2 one-zone time-dependent modelling is discussed and the model parameters of a representative test case blazar in Section 3.3. In Section 3.4 the method for generating variations for simulating variability is explained.

3.1 The Leptonic Scenario

In the leptonic scenario it is assumed that electrons and positrons[1] are responsible for the radiation. A cold proton background that is not energetic enough to contribute significantly to detected emission is also assumed to be present to adhere to charge neu-

[1]Collectively referred to as just "electrons" in the rest of the text. This is due to the radiation mechanisms of electrons and positrons being practically identical.

Table 3.1: General symbol list

Symbol	Description
c	speed of light
β	fraction of the speed of light
γ	Lorentz factor
e	elementary charge
m_e	electron mass
ϵ	photon energy as fraction of electron rest mass energy
n_i	number density of particle species i
u_i	energy density of i
Ω	solid angle
B	magnetic field

trality. Based on these assumptions all the mechanisms focus on motion and radiative output of electrons.

3.1.1 Synchrotron Emission

From Electrodynamics it is known that accelerated charged particles radiate. Synchrotron radiation is produced by relativistic charged particles that are accelerated by magnetic fields. The low-energy hump in the broadband SED is produced by synchrotron radiation of electrons.

The radiation power of a single electron per photon frequency per electron energy averaged over all pitch angles is given by Crusius and Schlickeiser (1986):

$$P_\nu^{\text{sync}}(\gamma) = \frac{\sqrt{3}\pi e^3 B}{2m_e c^2} x\text{CS}(x), \tag{3.1}$$

where $x = \nu/\nu_\text{c}$ is the ratio of photon and critical frequency, $\nu_c = \frac{3eB}{4\pi m_e c}\gamma^2$ and $\text{CS}(x)$ is a combination of Whitaker functions. Calculating the synchrotron power can thus be computationally quite expensive and is often approximated with either an asymptotic equation (3.2) or delta function (3.3)(Böttcher et al., 2012):

$$P_\nu^{\text{sync, asymp}}(\gamma) = \frac{32\pi c}{9\Gamma(4/3)}\left(\frac{e^2}{m_e c^2}\right)^2 u_B \beta^2 \gamma^2 \frac{\nu^{1/3}}{\nu_\text{c}^{4/3}} e^{-\nu/\nu_\text{c}} \tag{3.2}$$

$$P_\nu^{\text{sync, }\delta}(\gamma) = \frac{32\pi c}{9}\left(\frac{e^2}{m_e c^2}\right)^2 u_B \beta^2 \gamma^2 \delta(\nu - \nu_\text{c}). \tag{3.3}$$

The emissivity coefficient of synchrotron emission is calculated as:

$$j_\nu^{\rm sync}(t) = \frac{1}{4\pi}\int_1^\infty d\gamma n_e(\gamma,t)\cdot P_\nu^{\rm sync}(\gamma). \tag{3.4}$$

The particle energy-loss rate of the electrons is calculated as:

$$\left(\frac{d\gamma}{dt}\right)_{\rm sync} = -\frac{4c}{3}\sigma_T\frac{u_B}{m_e c^2}\beta^2\gamma^2. \tag{3.5}$$

Equations (3.2), (3.3) & (3.5) show that the radiated energy scales with the electron energy, $E_{\rm rad}\propto\gamma^2$. It can also be deduced that the cooling time scale $t_{\rm cool}^{\rm sync}\approx\gamma\left|\frac{d\gamma}{dt}\right|_{\rm sync}^{-1}$ also scales with electron energy $t_{\rm cool}^{\rm sync}\propto\gamma^{-1}$. Therefore higher energy electrons radiate more energy on smaller timescales compared to low-energy electrons.

3.1.2 Synchrotron Self-Absorption

Emission can also be absorbed by Synchrotron Self-Absorption (SSA). Having the restrictive assumption that the energy of the absorbed photon is much less than the interacting electron $\epsilon\ll\gamma$ the absorption coefficient is calculated as (Böttcher et al., 2012):

$$\alpha(\nu,t) = \frac{-1}{8\pi m_e\nu^2}\int_1^\infty d\gamma P(\nu,\gamma)\gamma^2\frac{\partial}{\partial\gamma}\left(\frac{n_e(\gamma,t)}{\gamma^2}\right). \tag{3.6}$$

For electrons distributed as a power law with particle energy with index q

$$\alpha(\nu,t) = \frac{q+2}{8\pi m_e\nu^2}\int_1^\infty d\gamma P(\nu,\gamma)\frac{n_e(\gamma,t)}{\gamma}. \tag{3.7}$$

Substituting the synchrotron delta-function approximation (Eq. 3.3) into the equation as $P(\nu,\gamma)$ the following result is obtained

$$\alpha(\nu,t) = \frac{q+2}{18\pi m_e}\left(\frac{3e}{4\pi m_e c}\right)^{\frac{q-2}{2}}\left(\frac{e}{m_e c^2}\right)^2 B^{\frac{q+2}{2}}\nu^{-\frac{q+4}{2}}. \tag{3.8}$$

From this it is clear that SSA scales strongly with magnetic field strength. It is also strongest for low photon frequencies.

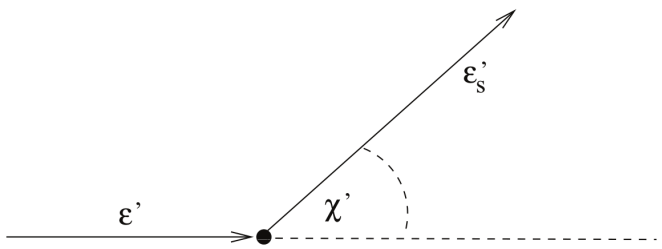

Figure 3.1: Geometry of a collision between an electron and photon in the ERF. Illustration from Böttcher et al. (2012).

3.1.3 Compton Scattering

The collision of a high-energy relativistic particle and a low-energy photon which produces a high-energy photon and a particle with lower energy than initially is known as Inverse Compton (IC) scattering. In effect energy from the relativistic electron is transferred to the photon. The model has a whole population of high-energy relativistic electrons scattering a field of low-energy photons. The high-energy hump in the SED is due to this mechanism.

In the Electron Rest Frame (ERF[2]) the calculations start off with a single photon with energy $\epsilon' = E'_{\rm ph}/(m_{\rm e}c^2)$ colliding with an electron. The scattering angle of the photon after the collision is χ'.

Using the conservation of momentum the scattered photon energy $\epsilon'_{\rm s}$ is calculated in terms of its initial energy:

$$\epsilon'_{\rm s} = \frac{\epsilon'}{1+\epsilon'(1-\cos\chi')}. \tag{3.9}$$

For photon energies $\epsilon' \ll 1$, also known as the Thomson regime, the interactions are approximately elastic. For photon energies $\epsilon' \gg 1$, known as the Klein-Nishina (KN) regime, the interactions are inelastic.

For the calculations with electron populations and photon fields the KN differential cross-section $\frac{d\sigma_{\rm C}}{d\epsilon_{\rm s} d\Omega_{\rm s}}$ is used to obtain the relevant quantities. The emissivity coefficient is calculated with (Böttcher et al., 2012):

$$j^{\rm C}_{\nu}(\epsilon_{\rm s},\Omega_{\rm s}) = \oint d\Omega_{\rm ph} \oint d\Omega_{\rm e} \int_0^{\infty} d\epsilon \int_1^{\infty} d\gamma \; h\epsilon_{\rm s} \left[n_{\rm ph}(\epsilon,\Omega_{\rm ph}) \; n_{\rm e}(\gamma,\Omega_{\rm e}) \; c(1-\beta\cos\theta) \; \frac{d\sigma_{\rm C}}{d\epsilon_{\rm s} d\Omega_{\rm s}} \right], \tag{3.10}$$

[2]Quantities in the ERF are primed.

where the factor in brackets represents the number of collisions per volume element, per second, per scattered energy and per solid angle for given $\epsilon, \gamma, \Omega_{\rm ph}$ and $\Omega_{\rm e}$. The angle between an electron and photon prior to a collision is θ. Multiplying the collision rate with the appropriate energy term and then integrating over all the electron and photon populations' solid angles and energies yield the desired coefficient.

This demonstrates that the KN cross-section $\frac{d\sigma}{d\epsilon_{\rm s} d\Omega_{\rm s}}$ is the quantity of interest for such calculations. In the ERF this is given by (Jauch and Rohrlich, 1976)

$$\frac{d\sigma_{\rm C}}{d\epsilon'_{\rm s} d\omega'_{\rm s}} = \frac{r_{\rm e}^2}{2}\left(\frac{\epsilon'_{\rm s}}{\epsilon'}\right)^2\left(\frac{\epsilon'_{\rm s}}{\epsilon'} + \frac{\epsilon'}{\epsilon'_{\rm s}} - \sin^2\chi'\right)\delta\left(\epsilon'_{\rm s} - \frac{\epsilon'}{1+\epsilon'[1-\cos\chi']}\right). \tag{3.11}$$

However, these quantities are needed in the lab frame of reference[3] which requires a transformation. The cross-section for an electron with energy γ in the lab frame is given as

$$\frac{d\sigma_{\rm C}}{d\epsilon_{\rm s} d\Omega_{\rm s}} = \delta_{\rm s}(\gamma)\frac{d\sigma_{\rm C}}{d\epsilon'_{\rm s} d\Omega'_{\rm s}}, \tag{3.12}$$

where $\delta_{\rm s}(\gamma) = \epsilon_{\rm s}/\epsilon'_{\rm s} = (\gamma[1-\beta\cos\theta_{\rm s}])^{-1}$ is the Doppler factor with $\theta_{\rm s}$ the angle between electron and photon after scattering.

The particle energy-loss rate is given by the following equation

$$\left(\frac{\partial\gamma}{\partial t}\right)_{\rm C} = \oint d\Omega_{\rm ph}\oint d\Omega_{\rm s}\int_0^\infty d\epsilon\int_0^\infty d\epsilon_s\ (\epsilon_{\rm s}-\epsilon)\left[n_{\rm ph}(\epsilon,\Omega_{\rm ph})\ c(1-\beta\cos\theta)\ \frac{d\sigma_{\rm C}}{d\epsilon_{\rm s}d\Omega_{\rm s}}\right]. \tag{3.13}$$

The calculations can be simplified by making assumptions that reduce the KN cross-section to the following delta-function approximation:

$$\left.\frac{d\sigma_{\rm C}}{d\epsilon_{\rm s} d\Omega_{\rm s}}\right|_\delta = \sigma_{\rm T}\delta(\Omega_{\rm e}-\Omega_{\rm s})\delta(\epsilon_{\rm s}-\epsilon\gamma^2(1-\beta\cos\theta)) \tag{3.14}$$

The first assumption for this simplification is relativistic beaming effects. A relativistic electron with energy γ moving through an isotropic distribution of photons will encounter half of them in a cone with opening angle $\frac{1}{\gamma}$ in its ERF. Also scattered photons are strongly beamed along the electron's direction of motion. Therefore only head-on collisions with scattering direction in the electron's direction of motion are considered hence when $\Omega_{\rm e} = \Omega_{\rm s}$ such that $\delta(\Omega_{\rm e}-\Omega_{\rm s}) = 1$ in Equation (3.14).

Secondly only scattering in the Thomson regime is considered. The total KN cross-section then reduces to the Thomson cross-section and the scattered photon energy

[3]Unprimed quantities.

evaluates to $\epsilon_s \approx \epsilon\gamma^2(1-\beta\cos\theta)$ hence $\sigma_T\delta(\epsilon_s - \epsilon\gamma^2(1-\beta\cos\theta))$ in Equation (3.14). It should be noted that this will produce slightly over predicted spectra in the KN regime, however, the approximation obtained from the simplification still provides an effective way to make predictions.

The general energy-loss rate using the delta-function approximation is:

$$\left(\frac{d\gamma}{dt}\right)_{\rm C} \approx \frac{4}{3}c\sigma_T\frac{u_{\rm ph}}{m_e c^2}\gamma^2. \tag{3.15}$$

This is similar to synchrotron energy-loss rate where instead of a dependence on the magnetic energy density the Compton particle energy-loss rate depends on photon energy density. The energy-loss rate also scales with γ^2; thus the cooling time scale will also be proportional to γ^{-1}.

$$t^{\rm C}_{\rm cool} = \gamma\left|\frac{d\gamma}{dt}\right|^{-1}_{\rm C} \propto \gamma^{-1}. \tag{3.16}$$

The Compton radiation spectrum is obtained from the electron population and photon field in the emission region. The electron population is the same as for the synchrotron radiation. The photon field on the other hand is a combination of photons from a wide range of sources.

The first photon field source is the synchrotron emission produced by the emission region itself. The Compton scattering of the synchrotron emission is known as Synchrotron Self-Compton (SSC). This is also the only internal photon field source.

All other photon field sources are external or in other words outside the jet. These are the emission from the accretion disc, corona, BLR, NLR, and torus which is commonly referred to External Compton (EC) scattering.

3.1.4 $\gamma\gamma$ Absorption

High-energy γ-rays ($\gtrsim 100\,\mathrm{GeV}$) along with lower-energy photons poses enough energy to annihilate and produce electron-positron pairs. This process is referred to as $\gamma\gamma$ absorption or pair production.

For this interaction the threshold energies of the photons can be calculated from the normalised velocities of the e^-e^+ pair in the center of momentum frame [4] (Böttcher et al., 2012).

[4] In this frame the momentum of the e^- and e^+ is equal.

$$\beta_{\rm cm} = \sqrt{1 - \frac{2}{\epsilon_1 \epsilon_2 (1 - \cos\theta)}} \tag{3.17}$$

where ϵ_1 and ϵ_1 is the energy of the two photons, and θ the angle of interaction between the photons. The velocities are required to be real-valued which therefore yields the threshold energy of the γ-ray with respect to the lower-energy photon.

$$\epsilon_1 \leq \frac{2}{\epsilon_2 (1 - \cos\theta)} \tag{3.18}$$

The $\gamma\gamma$ absorption cross-section written as a function of $\beta_{\rm cm}$ is given by (Jauch and Rohrlich, 1976):

$$\sigma_{\gamma\gamma} = \frac{3}{16}\sigma_{\rm T}(1 - \beta_{\rm cm}^2)\left([3 - \beta_{\rm cm}^4]\ln\left[\frac{1 + \beta_{\rm cm}}{1 - \beta_{\rm cm}}\right] - 2\beta_{\rm cm}[2 - \beta_{\rm cm}^2]\right) \tag{3.19}$$

With the $\gamma\gamma$ absorption cross-section and a photon field $n_{\rm ph}(\epsilon_2, \Omega, x)$ for Ω the solid angle and $x = \epsilon_1\epsilon_2(1 - \cos\theta)$ the $\gamma\gamma$ absorption opacity can be calculated over path length l:

$$\tau_{\gamma\gamma} = \int_0^l dx \int_{4\pi} d\Omega \int_{\frac{2}{\epsilon_1(1-\cos\theta)}}^{\infty} d\epsilon_2 \left[(1 - \cos\theta) n_{\rm ph}(\epsilon_2, \Omega, x)\sigma_{\gamma\gamma}(\epsilon_1, \epsilon_2, \theta)\right[\tag{3.20}$$

The observed emission from an emission region subject to $\gamma\gamma$ absorption under th assumption of homogeneity of physical conditions within can then be calculated as:

$$F_\nu^{\rm obs} \approx F_\nu^{\rm int}\frac{1 - e^{\tau_{\gamma\gamma}}}{\tau_{\gamma\gamma}} \tag{3.21}$$

with $F_\nu^{\rm obs}$ and $F_\nu^{\rm int}$ the observed and intrinsic flux.

3.2 One-Zone Time-Dependent Modelling

In the one-zone model we assume one homogeneous blob of particles with radial size R moving at relativistic speed, quantified by the bulk Lorentz factor Γ, along the jet axis of the blazar. The angle of the jet with respect to our line of sight is $\theta_{\rm obs}$. The emission region contains a homogeneous isotropic magnetic field B and the particles discussed in the leptonic scenario (Section 3.1).

The time evolution of the electron population and photon field in the emission region

is calculated with coupled differential equations in the co-moving frame of reference (CMF). From this the observable emission is calculated.

The time-evolution Fokker-Planck (FP) equation for the electron population is:

$$\frac{\partial n_e(\gamma,t)}{\partial t} = \frac{\partial}{\partial \gamma}\left[\frac{\gamma^2}{(a+2)\cdot t_{\rm acc}}\frac{\partial n_e(\gamma,t)}{\partial \gamma}\right] - \frac{\partial}{\partial \gamma}(\dot{\gamma}_{\rm rad}\cdot n_e(\gamma,t)) + Q(\gamma,t) - \frac{n_e(\gamma,t)}{t_{\rm esc}}. \quad (3.22)$$

The time evolution differential equation for the photon field is:

$$\frac{\partial n_{\rm ph}(\nu,t)}{\partial t} = \frac{4\pi}{h\nu} j_\nu(t) - n_{\rm ph}(\nu,t)\left(\frac{1}{t_{\rm esc,ph}} + \frac{1}{t_{\rm abs,ph}}\right). \quad (3.23)$$

In the electron FP equation (3.22) the first term denotes the diffusion coefficient of electrons in energy space. This diffusion is due to interactions with magnetohydrodynamic (MHD) turbulence. The diffusion in the model resembles hard sphere scattering in this work. This leads to energy-independent stochastic acceleration and the normalisation term $1/([a+2]t_{\rm acc})$ in which $a = \frac{v_s^2}{v_A^2}$ with v_s and v_A being the shock and Alvèn speeds.

The second term denotes the energy loss due to radiation. This accounts for the losses due to synchrotron and IC.

The emission region is continuously injected with electrons; thus the injection term $Q(\gamma,t)$. It is assumed that the injected electron spectrum is of the form of a power-law:

$$Q(\gamma,t) = Q_0(t)\gamma^{-q} H(\gamma;\gamma_{\rm min},\gamma_{\rm max}). \quad (3.24)$$

$H(\gamma;\gamma_{\rm min},\gamma_{\rm max})$ is the Heaviside function which is 1 for $\gamma_{\rm min} \leq \gamma \leq \gamma_{\rm max}$ and 0 otherwise. Q_0 is the normalisation factor which is calculated with $Q(\gamma,t)$ normalised to the electron injection luminosity $L_{\rm inj}$ and the volume of the emission region V_b:

$$Q_0 = \begin{cases} \frac{L_{\rm inj}(t)}{V_b m_e c^2}\frac{2-q}{\gamma_{\rm max}^{2-q}-\gamma_{\rm min}^{2-q}} & \text{if } q \neq 2 \\ \frac{L_{\rm inj}(t)}{V_b m_e c^2 \ln\left(\frac{\gamma_{\rm max}}{\gamma_{\rm min}}\right)} & \text{if } q = 2 \end{cases} \quad (3.25)$$

The final term accounts for losses of particles escaping the emission region. The escape timescale is proportionate to the emission region light crossing timescale $t_{\rm esc} \propto R/c$.

In the time evolution differential equation (3.23) of the photon field the first term on the right hand side accounts for all the emission processes. The second term is the losses due to absorption of photons by SSA and $\gamma\gamma$-absorption as well as the photons

Table 3.2: Baseline model parameters used in the leptonic code. Similar to that of Zacharias et al. (2017).

Definition	Symbol	Value
Magnetic field of the emission region	B	3.70 G
Blob radius	R	2.50×10^{16} cm
Escape time scale	$t_{\rm esc}$	10.0 R/c
Ratio of the acceleration to escape time scales	η	1.00
Redshift to the source	z	1.037
Minimum Lorentz factor for the electron injection spectrum	$\gamma_{\rm min}$	1.0×10^{1}
Maximum Lorentz factor for the electron injection spectrum	$\gamma_{\rm max}$	3.0×10^{3}
Bulk Lorentz factor for the blob	Γ	35.0
Observing angle relative to the axis of the BH jet	$\theta_{\rm jet}$	2.86×10^{-2} rad
Electron injection index	q	2.4
Injection luminosity for the electron spectrum	Q	2.40×10^{43} erg·s^{-1}
Mass of the supermassive black hole	$M_{\rm BH}$	$8.5 \times 10^{8} M_{\odot}$
Eddington ratio	$l_{\rm edd}$	3.50×10^{-1}
Initial location of the blob along jet axis	d	6.50×10^{17} cm
Radius of the BLR	$R_{\rm BLR}$	6.70×10^{17} cm
Effective temperature of the BLR	$T_{\rm BLR}$	5.0×10^{4} K
Effective luminosity of the BLR	$L_{\rm BLR,\ eff}$	4.14×10^{45} erg·s^{-1}

that escape the region.

The observable broadband emission is then calculated from the CMF solutions of $n_e(\gamma, t)$ and $n_{\rm ph}(\nu, t)$ in Equations (3.22) and (3.23) at each time step t_k.

$$f_\nu^{\rm obs}(t_k^{\rm obs}) = \nu^{\rm obs} F_\nu^{\rm obs}(t_k^{\rm obs}) = \frac{h\nu^2 n_{\rm ph}(\nu, t_k)\delta^4 V_{\rm b}}{4\pi d_L^2 t_{\rm esc,ph}} \tag{3.26}$$

h is Planck's constant and d_L and $\delta = \Gamma^{-1}(1 - \beta_\Gamma \cos\theta)^{-1}$ is the luminosity distance and the Doppler factor of the emission region. Quantities in the observer's frame are labeled with "obs". Therefore, $f_\nu^{\rm obs} = \nu^{\rm obs} F_\nu^{\rm obs}(t_k^{\rm obs})$ is the flux power at frequency $\nu^{\rm obs}$ for the k'th time step in the observer's frame.

3.3 Model Parameters

As mentioned in Section 1.2 the two peaks in the SED are due to synchrotron and IC emission produced by relativistic electrons. This work uses the time-dependent leptonic model code of Diltz and Böttcher (2014) adapted by Zacharias et al. (2017) to model long-term time-dependent leptonic blazar emission.

The parameters used are contained in Table 3.2 and represents the flat spectrum radio quasar (FSRQ) CTA102. Here Eddington ratio indicates the ratio between the

accretion disc luminosity and the Eddington luminosity which is the luminosity limit where radiation pressure produced by the accretion disc emission is equal to the gravitational force of the accreting compact object, the SMBH of CTA102 in this case. The SED of this blazar is adequately explained by the leptonic model which makes it a perfect representative test case. Baseline parameters similar to the low-state parameters from Zacharias et al. (2017) are implemented. The steady-state SED produced by the model for the mentioned parameters is shown in Figure 3.2.

In this code the emission region is assumed to be a single, homogeneous blob in relativistic motion along the jet with an isotropic, homogeneous magnetic field. The electron distribution and radiation are calculated in the CMF and transformed to the observer's frame by taking redshift and Doppler boosting into account.

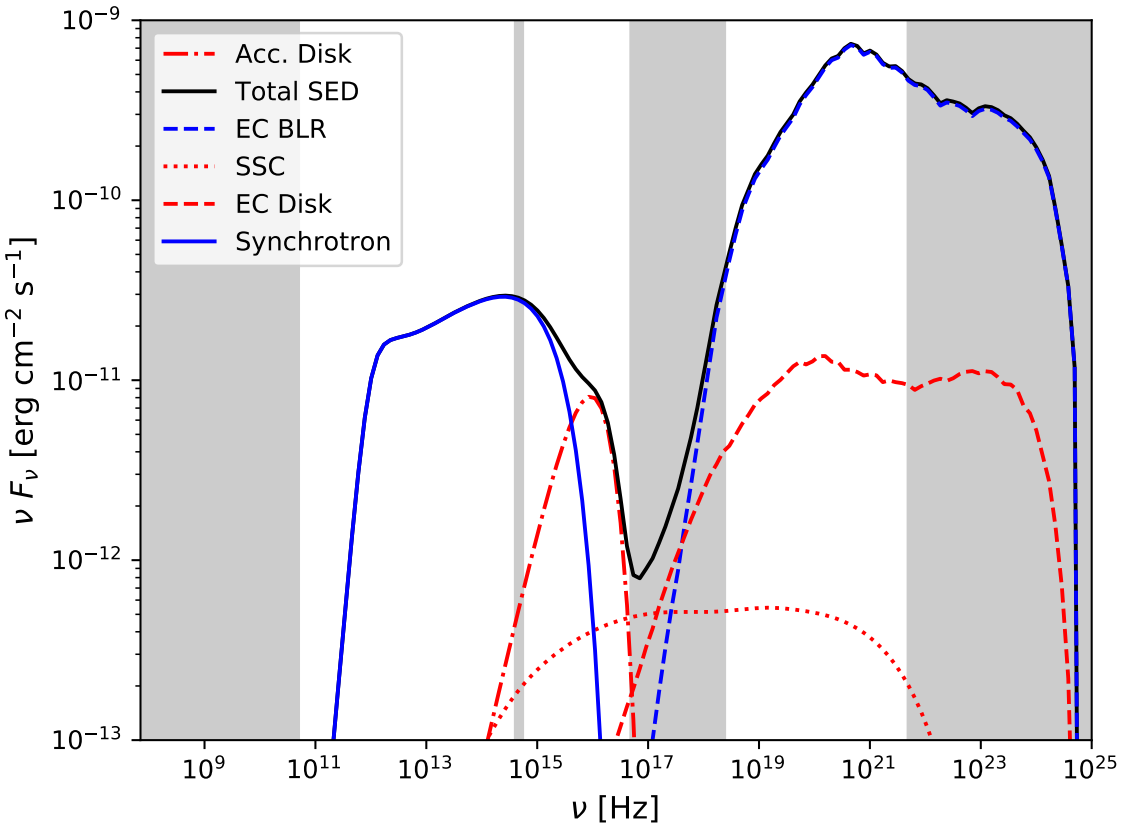

Figure 3.2: Steady-state SED. Flux components are described in the legend. The shaded areas indicate the ranges used to calculate the integrated fluxes.

The light curves produced by the code are the integrated fluxes in ranges of 73 MHz - 50 GHz (radio), R-band (optical), 0.2 - 10 keV (X-rays), 20 MeV - 300 GeV (γ-rays).

3.4 Generating Stochastic Variations

In this setup a method is needed to generate multiple variations that are stochastically dependent on a common property which can be controlled. As mentioned in Chapter 1 the variability in blazars as well as X-ray binaries is often characterised by red noise at high temporal frequencies. That is, the power at high temporal frequencies follows an inverse power-law with respect to the frequency. Since an inverse power-law cannot be maintained for infinitesimally low frequencies – there is some critical frequency at which the red noise will reduce to white noise. This critical frequency is not known for blazars.

The shape of the PSD is therefore the property we choose to control and use as seed to generate different variations. A Monte Carlo implementation is also required to make the generation process stochastic and therefore the algorithm developed by Timmer and König (1995) is employed to meet this requirement. The algorithm generates non deterministic linear time series. For a given frequency power spectrum a periodogram is generated in a stochastic manner and the Fourier transformed to produce a time series with randomized phases and amplitudes. A detailed explanation of the algorithm's implementation in this work follows in the next paragraphs.

In the algorithm one assumes an underlying spectrum, $S(f)$, for the variation. In this case a power-law spectrum $f^{-\alpha}$, typically found in the emission of X-ray binary systems, is used.

$$S(f) = f^{-\alpha}. \tag{3.27}$$

A periodogram, $p_k = p(f_k)$ for $k = \{1, N\}$ with N the number of points spaced Δf (arbitrary for the moment) apart in the frequency range, is obtained by calculating two normally-distributed random variables, $\mathscr{N}(\mu, \sigma^2)$, around the average, $\mu = 0$, and variance, $\sigma^2 = \frac{1}{2}S(f_k)$. Multiply one with $i = \sqrt{-1}$ and add them up to obtain a complex value. This ensures a randomised phase and amplitude for each frequency.

$$p_k = \mathscr{N}(0, \frac{1}{2}f_k^{-\alpha}) + i\mathscr{N}(0, \frac{1}{2}f_k^{-\alpha}). \tag{3.28}$$

The periodogram is thus proportional to the square root of half the spectrum, $p \propto \sqrt{f^{-\alpha}}$. The PSD is $P(f) = |p(f)|^2 \propto f^{-\alpha}$. Calculating the FFT of the periodogram $\{p_k\}_1^N$ yields a generic time series $\{x_k\}_1^N$ for a time step size of $\Delta t = (\Delta f N)^{-1}$:

$$\{x_k\}_1^N = \mathrm{FFT}[\{p_k\}_1^N]. \tag{3.29}$$

The time series real amplitudes typically range within $[-10, 10]$ in arbitrary units.

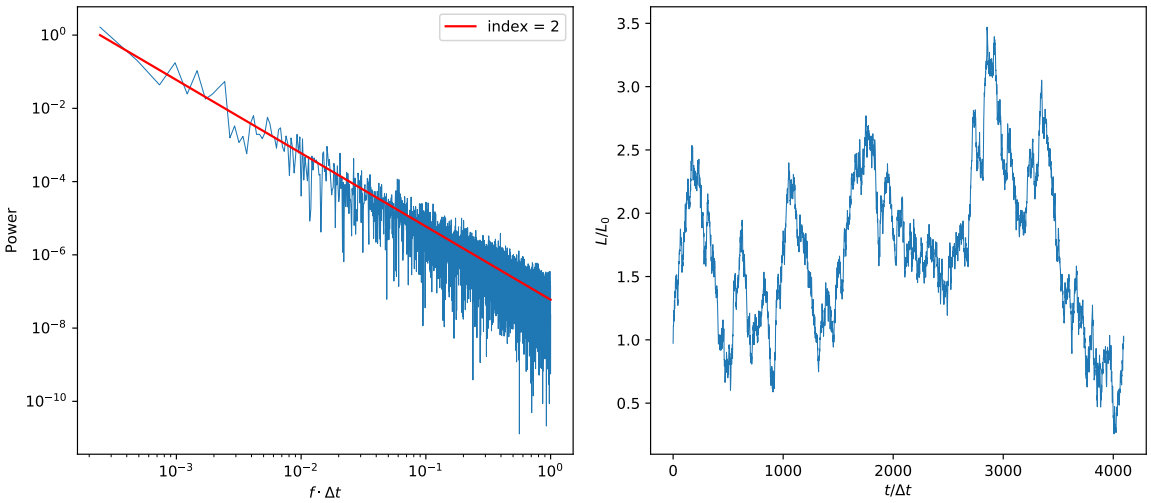

Figure 3.3: Typical variation generated by the method described in Section 3.4. *Left:* The PSD in blue obtained from the periodogram produced with the seed spectrum $S(f) = f^{-2}$ indicated in red. *Right:* The time series obtained from the FFT of the periodogram and amplitudes offset by ~ 2.4 to be suitable as a variation for injection luminosity.

It is further manipulated to represent the variation of each of the properties of the emission region chosen. The three parameter variations chosen for investigation are: electron injection luminosity, magnetic field strength and the electron spectral index in the emission region. For each time series three parameter variations are produced and used in separate realisations.

In the case of injection luminosity a constant is added to the variation such that the minimum value of the entire series is 0 $\mathrm{erg \cdot s^{-1}}$. This is also done for the magnetic field except that all minima are shifted to 0.1 G. For spectral index variation the amplitude range is changed to specifically fit within [-1, 1] by multiplying by a constant.

After these scalar manipulations each point in the time series of the injection luminosity and magnetic field is considered to be a scalar factor of the base parameter in the model. The variation in the model is then produced by changing the base value by the scalar factor value of the time series at each step. The time series for the spectral index, however, is not a scalar factor of the base value. Instead the value of the spectral index time series is added to the base electron spectral index at each step.

All of these manipulations do not affect the power index of the variation's PSD. Adding a constant shifts the series on the y-axis which only affects the value of the PSD at $f = 0$. This is of no concern since this value has to be ignored already to avoid computation errors when using a power-law. Multiplying with a constant on the other

hand effectively translates to multiplying the PSD with that same constant.

Furthermore, the time step size of the variations was kept at 2 h in the CMF and the total amount of steps to 4000. This then gives the variations a total duration of 8000 h in the emission region.

Chapter 4

Results and Discussion

Our results consist of light curves and SED snapshots from the leptonic variability model. The varied parameter is alternated between electron injection luminosity, magnetic field strength and electron spectral index. The light curves recovered for the input variations shown in Figure 3.3 are shown in Figure 4.1. Due to the relativistic motion of the emission region the total duration of the generated variations shrinks from 8000 hours in the CMF frame to 456 hours in the observer's frame. The curves show that there are clear differences across the different parameters varied.

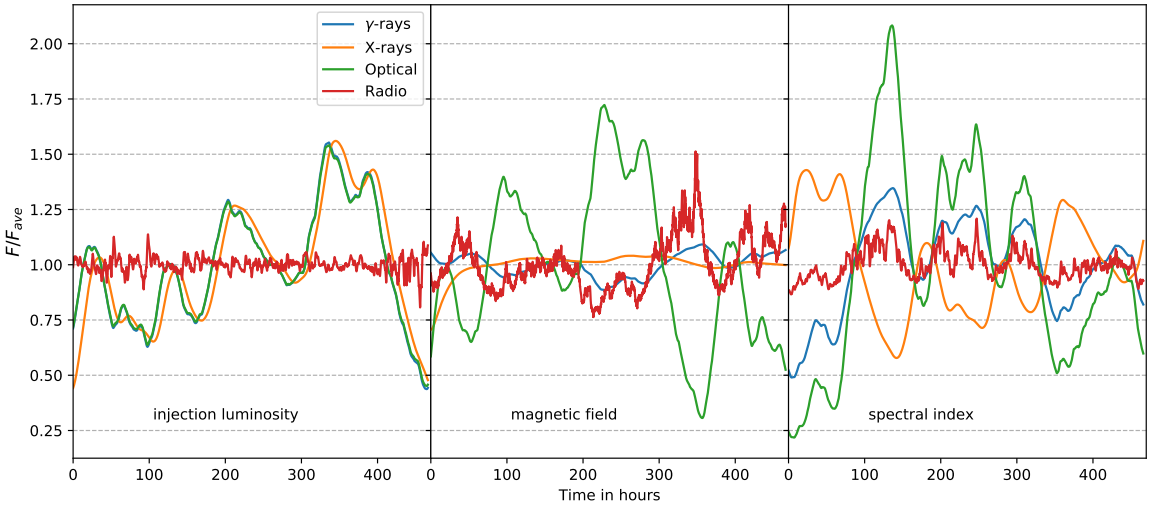

Figure 4.1: Light curves showing the variability as a result of the variations of Figure 3.3.

The variation of injection luminosity exhibits synchronised variability for the different wavelengths with the exception of radio. The light curves normalised to average flux for optical and γ-rays are practically identical. A delay in X-rays with respect to

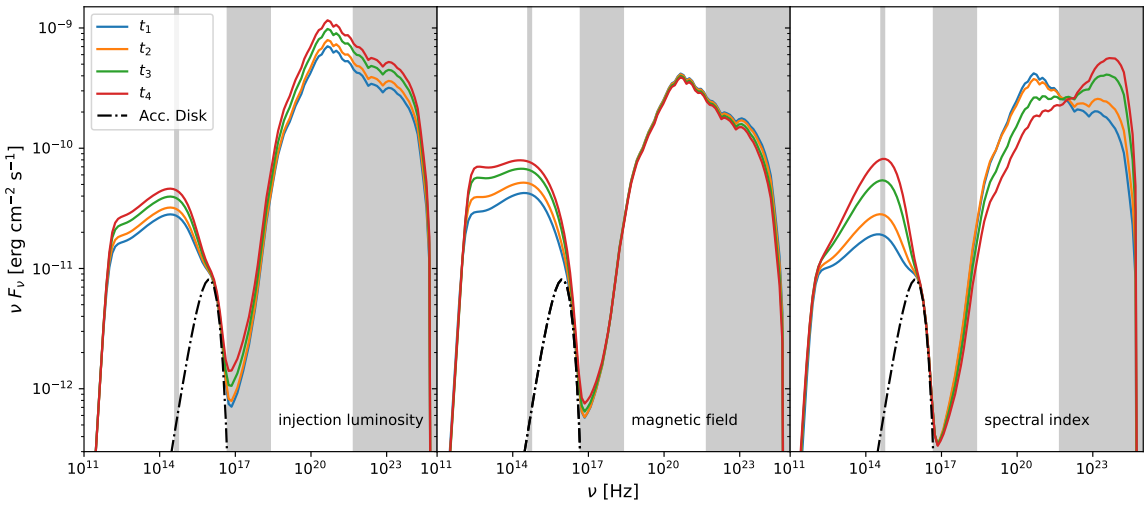

Figure 4.2: SED snapshots evenly-spaced in time during an increase for injection luminosity (left) and magnetic field (middle) and a hardening of spectral index (right). The time frames used are 291 - 332 hours for injection luminosity, 188 - 229 hours for magnetic field and 60 - 120 hours for spectral index.

those two wavelengths is also clearly visible. This is a consequence of differences in cooling time scales between the low (X-rays) and high-energy (optical and γ-ray) electrons responsible for the emission. The maximal ratio between the low (LE) and high-energy (HE) electron cooling time scales can be approximated with $t^{\mathrm{HE}}_{\mathrm{cool}}/t^{\mathrm{LE}}_{\mathrm{cool}} \approx \frac{\gamma_{\mathrm{max}}}{\gamma_{\mathrm{min}}} = 3 \times 10^2$. Large scale amplitude variations are eliminated in the radio light curve leaving only small amplitude variations. This is due to SSA in the radio waveband which will be discussed in more depth with the light curve PSDs and cross-correlations.

The resulting light curves for the variation of magnetic field show the sensitivity of synchrotron emission to these types of changes. A stronger magnetic field translates to more efficient cooling; thus synchrotron emission will rise while IC emission of external steady photon fields will fall. This seems to be the case with the optical and γ-ray light curves. However, SSC will increase due to an increase in the target photon field. The X-rays contain both an SSC and external IC component. The result is less volatile variability from two counteracting components.

Varying the spectral index while keeping injection luminosity constant is effectively redistributing electrons between high and low energies. Therefore there are visible correlations between the synchrotron and high-energy IC radiation (optical and γ-rays) produced by the high-energy electrons and apparent anti-correlation of those radiation components with the X-rays which are produced by the low-energy electrons.

With the SED snapshots in Figure 4.2 it is easier to comprehend the changes in

emission outlined earlier from the light curves. However, due to the severity of the SSA the wavebands affected by it do not present any significant changes in the SED snapshots. This includes the considered radio range in this work. Following explanations with regard to the snapshots will therefore only refer to the wavebands unaffected by SSA. The time frames used to produce the snapshots were chosen to be during a time of increase of the injection luminosity (291 - 332 hours) and magnetic field (188 - 229 hours), but a hardening of the spectral index (60 - 120 hours) in the observer's frame of reference. An increase in injection luminosity increases the energy spectrum across all bands (left panel). Stronger magnetic fields increase the synchrotron components significantly while the changes in the HE IC components are weaker in magnitude and decreasing. The variability due to a hardening of the spectral index in the synchrotron and IC components is comparable in magnitude to what is seen in synchrotron for the increasing magnetic field. The spectral hardening causes an increase in HE electrons which in turn significantly increases both the synchrotron and high-energy IC components while simultaneously decreasing the low-energy IC component due to the decrease in low-energy electrons. Nothing can be said about the low-energy synchrotron component since it is not visible in the snapshots due SSA.

We proceed to calculate the PSDs and cross-correlations of the light curves to give a more quantitative analysis of the variability. Comparing the PSDs and cross-correlations of the different wavelengths will show the differences needed to make undoubted distinctions on the cause of variability. The results, therefore, focus on the PSDs and the cross-correlations.

4.1 Power Spectral Densities

Multiple realisations of variability with variations from a common seed PSD index α were averaged to reduce noise. The average PSDs of 10 realisations are presented in Figure 4.3 compared to the seed spectrum.

The PSDs for input index $\alpha = 2.0$ (Figure 4.3, left panel) follow the input variations closely except for radio. For input index $\alpha = 2.5$ (Figure 4.3, right panel) a deviation from the input variation is noticeable in all wavebands contrary to the results found for $\alpha = 2.0$. The light curve PSD indices are harder than the seed variation. Also contrary to the case of $\alpha = 2.0$ the X-rays have a slightly different index compared to its optical and γ-ray counterparts.

The optical, X-ray and γ-ray PSDs do not show large deviations from the underlying variation PSD index of any of the parameters. In contrast, there are significant

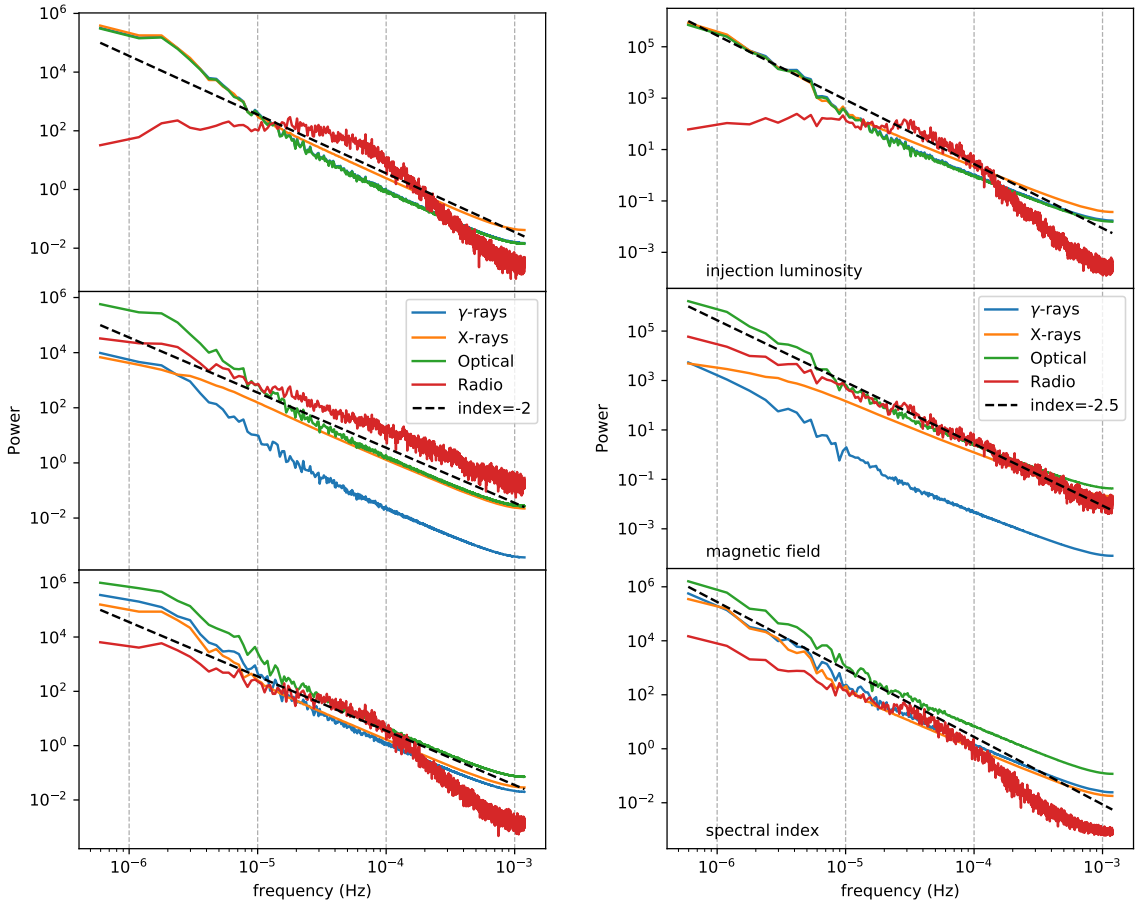

Figure 4.3: Average PSDs for 10 variations.

differences in the radio PSD depending on the varied parameter. For magnetic field variations the radio PSD behaves similar to the other wavelengths. The power in the longest time scale variations is suppressed in the radio PSD for the injection luminosity variations and slightly for spectral index variations. It appears that at approximately the minimum variability time scale $t = 13.47\,\mathrm{h} \Leftrightarrow f \approx 2.06 \times 10^{-5}\,\mathrm{s}^{-1}$ there is a break in these PSDs. These differences in the radio PSDs are due to the impact the varied parameters have on the strong SSA the considered radio waveband is subjected to in this model. Further discussions follow with the cross correlation results in the next section.

From a qualitative perspective the optical, X-ray and γ-ray PSDs do not present a way to distinguish between the varied parameter in question. Radio wavebands affected by strong SSA on the other hand do present distinctive features.

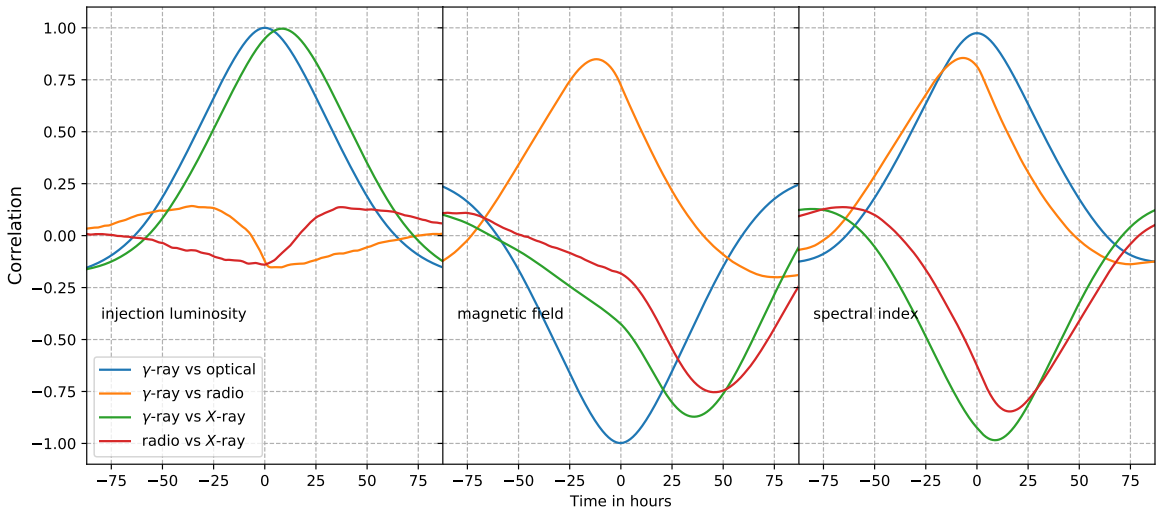

Figure 4.4: Average cross-correlations for the output light curves of 10 realisations.

4.2 Cross-correlations

At the beginning of this chapter the possible correlations and anti-correlations are briefly mentioned. The cross-correlation function allows us to quantify correlations and calculate time lags between the variability in different wavebands. Figure 4.4 shows the cross-correlations for the three variations. Table 4.1 contains the quantities of the cross-correlation strength and time lag for each waveband pair. This is again an average of 10 different realisations. The optical and γ-rays are almost perfectly correlated or anti-correlated ($\simeq \pm 1.0$) in each case with no time lags except for magnetic field variations which show that optical precedes γ-rays with 13.98 min (the time of two time steps). This consistency of strong correlations and small time lags is a confirmation that the emission is produced by electrons in a common energy range, that is highest energies. Due to this consistency the optical correlations with other wavebands are omitted for clarity since it will always mimic correlations with γ-rays perfectly.

For injection luminosity variations between optical, X-rays and γ-rays are perfectly correlated. The time delay between X-rays and γ-rays thus confirm the longer cooling time scales of the low-energy electrons producing the X-rays compared to the high-energy electrons producing optical via synchrotron and γ-rays via IC. The radio frequencies subject to SSA are not correlated to any of the other considered wavelengths for the injection luminosity variations. This indicates that the effect of variating injection luminosity in SSA affected wavebands counteracts itself. An increase would provide more particles for radiation mechanisms which for radio is synchrotron, but this also enhances absorption similarly and vice versa.

Table 4.1: Time delays and correlation strength of cross-correlations in Figure 4.4 Delays are given in hours.

Wavebands	**Delay (in hours)**	**Correlation strength**
Injection luminosity		
γ-ray vs optical	0.00	1.00
γ-ray vs radio	7.57	-0.15
γ-ray vs X-ray	8.39	1.00
radio vs X-ray	0.00	-0.14
Magnetic field		
γ-ray vs optical	-0.23	-1.00
γ-ray vs radio	-12.00	0.85
γ-ray vs X-ray	35.77	-0.87
radio vs X-ray	45.78	-0.75
Spectral index		
γ-ray vs optical	0.00	0.97
γ-ray vs radio	-6.76	0.86
γ-ray vs X-ray	8.85	-0.98
radio vs X-ray	15.96	-0.85

Electron cooling rates from synchrotron and IC of BLR photons are governed by the magnetic and BLR co-moving energy densities. Therefore there is a shift in the ratio of fluxes between synchrotron and IC/BLR with changes in the magnetic field. This is the reason for the anti-correlation between optical and γ-rays. Stronger magnetic fields are more efficient at cooling electrons which reduces high-energy electrons for IC scattering. This is supported by the fact that the γ-rays are delayed by $0.23\,\mathrm{h} = 14\,\mathrm{min}$ with respect to optical. The synchrotron emission reacts faster to magnetic field changes since it directly depends on it. The IC/BLR on the other hand has a weaker, indirect dependence on these changes through the electron population that is cooled by synchrotron. The weaker anti-correlation between γ-rays and X-rays (alternatively a correlation between optical and X-rays) can be attributed to the SSC and IC/BLR having counteracting effects for changing magnetic fields. That is, an increase in magnetic field causes an increase in SSC but a decrease in IC/BLR and vice versa, however, of the two components SSC is more significant in this case which is inferred from the anti-correlation. The time delay produced by cross correlations with X-rays are much more substantial

than other varying parameters. Not only does the difference in cooling time scales play a role in this as before, but as discussed earlier delays between synchrotron and IC emission should also be accounted for. These combined time scales and delays caused the delay of 35.77 h in γ-ray vs X-ray. In spite of this, it should be noted that the X-ray light curve itself presents little variation in this case and might not even be significant enough for detection. From the γ-ray vs optical cross correlation it is deduced that the γ-ray flux drops with magnetic field increases. The radio bands under severe SSA will also drop in flux since magnetic field increases enhance SSA, hence the significant correlation between γ-rays and radio. The same argument regarding dependence on magnetic field justifying the time delays between synchrotron and IC also holds for SSA and IC which leads the 12 hour time delay of γ-rays with respect to radio.

The transmission of electrons between high and low energies as the effect of changes in spectral index has already been mentioned. The cross correlations for spectral index variation confirm this. Radiation produced by the high-energy electron spectrum (optical and γ-rays) are correlated, however, they are anti-correlated with X-rays produced by the low-energy electron spectrum. The correlation strength and time delays in the cross correlations between γ-rays, optical and X-rays are similar to the cross correlations found for the injection luminosity variations. The reason for this is that when considering the low- and high-energy electron spectra separately both injection luminosity and spectral index variations have similar effects on the spectrum. In the low-energy spectrum an increase in luminosity would be similar to a softening of the spectral index. However, in the high-energy spectrum this would be true for an increase in luminosity and a hardening of the spectral index. Contrarily, the cross correlations with radio show distinctly different behavior in comparison to its cross correlations counterparts for the injection luminosity variations. Consider the softening of the spectral index. This would increase the low-energy electrons which in turn provides more particles to produce synchrotron radiation in the radio bands as well as enhance the absorption. However, since the increase is due to a spectral softening the increase in particles becomes more significant toward the lowest end of the electron energy spectrum. The implications of this are that the increase of particles capable of absorption at a specific frequency is larger than the increase in electrons that produce the emission of that particular frequency. Thus, the softening of the spectral index increases SSA much more than production of synchrotron which leads to a decrease in flux, therefore it is moderately correlated to γ-rays and optical. Also it can be deduced that the time scales SSA effects are faster than synchrotron due to the time delay 6.76 h of γ-rays with respect to radio.

Chapter 5

Summary and Conclusions

We have successfully simulated variability with our model in which we assumed that the variability is caused by the variation of a single emission region environment variable. In this work we tested electron injection luminosity, magnetic field strength in the emission region and the spectral index of the electron population.

With respect to PSDs the variability found in the light curves across all wavebands was similar to the variations of the considered changing parameter. The radio light curve is the only exception to this, but this is attributed to the impact the parameter variations have on the strong SSA in this energy range. In theory light curve PSDs might be a tool one can use to predict variation trends for observed variability, however the precise cause would still remain unknown since there are no clear distinctions between the different parameters unless there are wavebands subject to significant SSA which could produce distinctive features.

Multi-wavelength cross correlations on the other hand presented a way to distinguish the rapidly changing environment parameter. The cross-correlation coefficients were distinctly different for different variation parameters for the considered waveband pairs. It also shows light curve time delays between different wavebands which arise from energy-dependent cooling time scales. This therefore shows more promise as a way to distinguish different parameter variations as the cause of variability.

Changing the electron injection luminosity modifies the particle budget for radiative processes over the entire electron spectrum which lead to synchronized changes confirmed by perfect correlations at all the considered wavelengths except radio. The strong SSA in radio suppressed the flux to such an extent that the radio could not be considered correlated to other wavelengths. This suppression of the flux was also seen in the radio PSD as a decrease in the strongest variation power for the longest time scales (smallest frequencies).

The variation of magnetic field strongly affects all components with synchrotron and SSA due to their direct dependence on it. The synchrotron cooling efficiency in turn affects the amount of electrons available to IC scattering which then results in a weak dependence. The variability in wavebands with synchrotron and SSA is also more significant compared to the IC wavebands. All light curve PSDs exhibit similar behavior and the cross correlations show anti-correlation between synchrotron and IC components. Our X-ray wave band which contains both SSC and IC show little variability in the light curve indicating counter-acting effects.

Hardening or softening of the electron spectral index redistributes electrons between low and high energies. Radiation produced by low-energy electrons is anti-correlated with radiation from the high-energy end of the electron spectrum. To some extent this leads to similar effects compared to a change in injection luminosity especially between optical and γ-rays. The suppression of variability seen for injection luminosity variations in radio is still present, evident from the radio PSD, but less significant. The reason for this is that in this case the change in SSA dominates the low-energy synchrotron and leads to the anti-correlation with radiation produced by low-energy electrons.

However, this work relied on the evenly-spaced nature of the generated data for the use of the FFT and classical correlation function to obtain the PSDs and cross-correlation coefficients. In practice contemporaneous multi-wavelength observational data are not this well sampled; thus using these tools for analyses presents a challenge. Therefore alternative techniques are required which do allow irregularly sampled data e.g. the Discrete Correlation Function (DCF) of Edelson and Krolik (1988).

Chapter 6

Outlook

Future prospects are to build on this work by developing a similar variability model for the hadronic emission case and investigate its variabiilty signatures for comparison to the variability of the leptonic emission.

The predictions of the models themselves need improvement which will be done by extending the variability model investigation. Possible extensions are: (1) expanding to more environment parameters as a variation variable and experimenting with simultaneous variations, (2) exploring additional variation PSD trends e.g. a broken power-law and exponential cut-off and (3) testing the prediction for other representative test cases of blazars.

The models can be refined by testing their predictions against observational data. Such an investigation can also lead to new insight on the nature of blazar jet variability and the environment from which it originates. Positive identification of the variability signatures found in this or future work for the hadronic scenario will lead to a better understanding of the changes occurring in the source. This will either confirm existing models on the origins of variability or open up the field for new ideas. Positive identification would also help settle the debate on jet composition and whether leptonic or hadronic models are best suited for blazar emission.

Currently most blazar emission models are simplistic by design to minimize free parameters. Investigation into variability provides an avenue for the improvement of these models. Better constraints on the model parameters from studying variability allow for the addition of more complexity to explore the physics fully. This principle can also be employed with polarization as well as the combination of polarization and variability.

Bibliography

Aartsen, M. et al. (2015). Evidence for astrophysical muon neutrinos from the northern sky with IceCube. *Physical Review Letters*, 115(8).

Aharonian, F. et al. (2007). An Exceptional Very High Energy Gamma-Ray Flare of PKS 2155-304. *ApJ*, 664:L71–L74.

Aharonian, F. et al. (2009). Simultaneous multiwavelength observations of the second exceptional γ-ray flare of PKS 2155-304 in July 2006. *A&A*, 502:749–770.

Araudo, A. T., Bosch-Ramon, V., and Romero, G. E. (2013). Gamma-ray emission from massive stars interacting with active galactic nuclei jets. *MNRAS*, 436(4):3626–3639.

Baring, M. G., Böttcher, M., and Summerlin, E. J. (2017). Probing acceleration and turbulence at relativistic shocks in blazar jets. *MNRAS*, 464(4):4875–4894.

Barkov, M. V., Aharonian, F. A., and Bosch-Ramon, V. (2010). Gamma-ray Flares from Red Giant/Jet Interactions in Active Galactic Nuclei. *ApJ*, 724(2):1517–1523.

Barkov, M. V. et al. (2012). Rapid TeV Variability in Blazars as a Result of Jet-Star Interaction. *ApJ*, 749(2):119.

Blandford, R. and Eichler, D. (1987). Particle acceleration at astrophysical shocks: A theory of cosmic ray origin. *Phys. Rep.*, 154(1):1–75.

Böttcher, M. and Dermer, C. D. (2010). Timing Signatures of the Internal-Shock Model for Blazars. *ApJ*, 711(1):445–460.

Böttcher, M. et al. (2013). Leptonic and Hadronic Modeling of Fermi-detected Blazars. *ApJ*, 768:54.

Böttcher, M., Harris, D. E., and Krawczynski, H. (2012). *Relativistic Jets from Active Galactic Nuclei*. Berlin: Wiley.

Bracewell, R. (1965). *The Fourier Transform and its applications*. McGraw-Hill.

Chatterjee, R. et al. (2012). Similarity of the Optical-Infrared and γ-Ray Time Variability of Fermi Blazars. *ApJ*, 749(2):191.

Crusius, A. and Schlickeiser, R. (1986). Synchrotron radiation in random magnetic fields. *A&A*, 164:L16–L18.

Cui, W. (1999). Temporal X-ray Properties of Galactic Black Hole Candidates: Observational Data and Theoretical Models. In Poutanen, J. and Svensson, R., editors, *High Energy Processes in Accreting Black Holes*, volume 161 of *Astronomical Society of the Pacific Conference Series*, page 97.

Della Ceca, R. et al. (1994). The properties of X-ray selected active galactic nuclei. 3: The radio-quiet versus radio-loud samples. *ApJ*, 430:533–544.

Diltz, C. and Böttcher, M. (2014). Time dependent leptonic modeling of Fermi II processes in the jets of flat spectrum radio quasars. *JHEAp*, 1:63–70.

Edelson, R. A. and Krolik, J. H. (1988). The discrete correlation function - A new method for analyzing unevenly sampled variability data. *ApJ*, 333:646–659.

Finke, J. D. and Becker, P. A. (2014). Fourier Analysis of Blazar Variability. *ApJ*, 791:21.

Goyal, A. et al. (2018). Stochastic Modeling of Multiwavelength Variability of the Classical BL Lac Object OJ 287 on Timescales Ranging from Decades to Hours. *ApJ*, 863:175.

Gültekin, K. et al. (2009). The M-σ and M-L Relations in Galactic Bulges, and Determinations of Their Intrinsic Scatter. *ApJ*, 698:198–221.

Guo, F. et al. (2016). Efficient Production of High-energy Nonthermal Particles during Magnetic Reconnection in a Magnetically Dominated Ion-Electron Plasma. *ApJ*, 818(1):L9.

Hubble, E. P. (1926). Extragalactic nebulae. *ApJ*, 64:321–369.

IceCube Collaboration et al. (2018). Neutrino emission from the direction of the blazar txs 0506+056 prior to the IceCube-170922a alert. *Science*, page eaat2890.

Jauch, J. M. and Rohrlich, F. (1976). *The Theory of Photons and Electrons*. Springer-Verlag, New York, Heidelberg, Berlin.

Kagan, D. et al. (2015). Relativistic Magnetic Reconnection in Pair Plasmas and Its Astrophysical Applications. *Space Sci. Rev.*, 191(1-4):545–573.

Kataoka, J. et al. (2001). Characteristic X-Ray Variability of TeV Blazars: Probing the Link between the Jet and the Central Engine. *ApJ*, 560(2):659–674.

Kellermann, K. I. et al. (1998). Sub-Milliarcsecond Imaging of Quasars and Active Galactic Nuclei. *AJ*, 115:1295–1318.

Magorrian, J. et al. (1998). The Demography of Massive Dark Objects in Galaxy Centers. *AJ*, 115:2285–2305.

Mastichiadis, A., Petropoulou, M., and Dimitrakoudis, S. (2013). Mrk 421 as a case study for TeV and X-ray variability in leptohadronic models. *MNRAS*, 434:2684–2695.

Nalewajko, K. et al. (2015). On the Distribution of Particle Acceleration Sites in Plasmoid-dominated Relativistic Magnetic Reconnection. *ApJ*, 815(2):101.

Oppenheim, A. V. and Schafer, R. W. (1975). *Digital signal processing*. Prentice-Hall Englewood Cliffs, N.J.

Papoulis, A. (1962). *The Fourier Integral and Its Applications*. McGraw-Hill.

Thiersen, H., Zacharias, M., and Böttcher, M. (2019). Characterising the long-term variability of blazars in leptonic models. *Galaxies*, 7(1).

Timmer, J. and König, M. (1995). On generating power law noise. *A&A*, 300:707.

Trippe, S. et al. (2011). The long-term millimeter activity of active galactic nuclei. *A&A*, 533:A97.

Urry, C. M. and Padovani, P. (1995). Unified Schemes for Radio-Loud Active Galactic Nuclei. *PASP*, 107:803.

Van der Klis, M. (2004). A review of rapid X-ray variability in X-ray binaries. *arXiv e-prints*, pages astro–ph/0410551.

Zacharias, M. et al. (2017). Cloud Ablation by a Relativistic Jet and the Extended Flare in CTA 102 in 2016 and 2017. *ApJ*, 851:72.

Zacharias, M. et al. (2019). The Extended Flare in CTA 102 in 2016 and 2017 within a Hadronic Model through Cloud Ablation by the Relativistic Jet. *ApJ*, 871(1):19.

Zweibel, E. G. and Yamada, M. (2009). Magnetic reconnection in astrophysical and laboratory plasmas. *Annual Review of Astronomy and Astrophysics*, 47(1):291–332.